INVITED ARTICLE FROM THE 2011 AND 2022 TEXAS ACADEMY OF SCIENCE TEXAS DISTINGUISHED SCIENTISTS

PEREGRINATIONS ON THE STUDY OF THE OPTICAL PROPERTIES OF NONSPHERICAL PARTICLES

Ping Yang[1] and George Kattawar[2]

[1]*Department of Atmospheric Sciences, Texas A&M University, College Station, TX 77843; 2022 Texas Distinguished Scientist*
Email: pyang@geos.tamu.edu

[2]*Department of Physics & Astronomy/Institute for Quantum Science & Engineering, Texas A&M University, College Station, TX 77843; 2011 Texas Distinguished Scientist*
Email: kattawar@tamu.edu

Dr. Ping Yang is *University Distinguished Professor* and holds the David Bullock Harris Chair in geosciences at Texas A&M University (TAMU), where he currently serves as the Senior Associate Dean for Research and Graduate Studies in the College of Arts and Sciences. He previously served as Department Head of Atmospheric Sciences (2012-2018) and Associate Dean for Research (2019-2022) in the College of Geosciences at TAMU. Dr. Yang has supervised/co-supervised 30 doctoral dissertations and 20 master's degree theses. He has published 366 peer-reviewed journal papers, thirteen invited book chapters, and four books. His publications have been cited 24,144 times (Google Scholar)/15,974 times (Web of Science) with an H-index of 79 (Google Scholar)/62 (Web of Science), as of 26 Sept 2023. His research focuses on light scattering, radiative transfer, and remote sensing. Since joining TAMU, Yang has been extramurally funded for 83 research projects.

Yang is a Fellow of the American Physical Society (APS), the Institute of Electrical and Electronics Engineers (IEEE), OPTICA (formerly the Optical Society of America), The Electromagnetics Academy, the American Geophysical Union (AGU), the American Meteorological Society (AMS), and the American Association for the Advancement of Science (AAAS). Yang received a number of awards/honors, including the *NASA Exceptional Scientific Achievement Medal* (2017), the *Ascent Award* by the AGU Atmospheric Science Section (2013), the *David and Lucille Atlas Remote Sensing Prize* by AMS (2020), and the *van de Hulst Light-Scattering Award* by Elsevier (2022), and a university-level faculty research award (2017) bestowed by The TAMU Association of Former Students (AFS). Dr. Yang was an elected member of the *International Radiation Commission* (IRC) under the International Association of Meteorology and Atmospheric Sciences (2012-2020) and was appointed as one of the 16 members of the U.S. *National Research Council-Space Studies Board's Committee on Earth Science and Applications from Space* (October 2018- June 2022). He has served as an editor of the Journal of the Atmospheric Sciences (2015-2020) and currently serves as an Editor-in-Chief of the Journal of Quantitative Spectroscopy & Radiative Transfer and an editor of the Journal of Geophysical Research-Atmospheres.

OPEN ACCESS DOI 10.32011/txjsci_75_1_TDS

Dr. George W. Kattawar is a Professor Emeritus in the Department of Physics & Astronomy and the Institute of Quantum Science & Engineering at Texas A&M University. He is an internationally renowned expert in radiative transfer and light scattering dealing with full Mueller matrix/Stokes vector processes. He has made significant contributions in using radiative transfer in such diverse areas as biomedical optics, planetary atmospheres, cloud and aerosol property studies related to climate studies, invisibility cloaking, ultrashort laser propagation in water, and anthrax detection. To list just a few among his seminal contributions, he was the first to show that the clouds of Venus were not water, which was the view held by two eminent scientists Carl Sagan and Richard Goody. It was this seminal work which led to the ultimate determination of the Venus cloud composition. He is one of the first researchers to apply Monte Carlo techniques to radiative transfer in planetary atmospheres. This technique is now being used by researchers all over the world and is also now being used in medical physics. He gave the first correct explanation of the "Ring effect" which had remained an enigma for over twenty years. This paper was designated by a world-renowned scientist at NASA to be the best paper of the decade in atmospheric science. Dr. Kattawar and his collaborators developed one of the most powerful time dependent, three-dimensional Monte Carlo codes capable of handling full Mueller matrix solutions for a coupled atmosphere-ocean system with a fully stochastic interface. This code will become the "Gold Standard" for all future researchers in biomedical, atmospheric, and oceanic optics. He is one of the first to show that nonspherical objects can be made totally invisible if the optical properties are selected in the right way. Dr. Kattawar received many awards and recognitions, including Fellow of the Optical Society of America (1976); Amoco Foundation Teaching Excellence Award (1981); Teacher/Scholar Award (1990), Nils Gunnar Jerlov Award (2014), and van de Hulst Light Scattering Award (2015); He was also elected for two, three-year terms on the Committee on Recommendations for U.S. Army Basic Scientific Research under the National Research Council. He is a former Associate Editor of the Journal of Geophysical Research-Oceans and a former Associate Editor of the Journal of Transport Theory and Statistical Physics. He was selected to be editor of the Society of Photo-Optical Instrumentation Engineers (SPIE) Milestone Series on "Multiple Scattering in Plane Parallel Atmospheres and Oceans: Techniques". He was selected (2009) to serve on the External Advisory Board of the Stevens Institute of Technology to assess their engineering and science programs. He was appointed as Academic Advisor of the Board of Directors of the Texas Academy of Science. He was selected by Applied Optics as one of the 50 most prolific authors in the last 50 years.

We are both humbled, honored, and grateful to the Texas Academy of Science for selecting us as recipients of the prestigious *Distinguished Texas Scientist* award. Over the years, we have been privileged to work with many outstanding graduate students, postdoctoral researchers, and early-career research scientists. They have inspired us to incessantly pursue excellence in teaching, research, and service for the research community, and they should equally share the honors which this award bestows. Below we briefly summarize our endeavor in studying the optical properties of nonspherical particles, which is in the

interdisplinary area of applied optics, electromagnetics, computational physics, radiative transfer, and remote sensing.

Dr. Ping Yang joined the Department of Atmospheric Sciences at Texas A&M University in 2001. Working with Prof. Gerald North, who was the department head at that time, Dr. Kattawar played an important role in recruiting Dr. Yang. Since then, Dr. Kattawar and Dr. Yang have been collaborating on research topics in light scattering, radiative transfer, and remote sensing. During this period of time, their combined research team had more than 20 members, including research scientists and graduate students. Among their cutting-edge contributions on many fronts, in what is to follow, we will give a short litany of their accomplishments in the area of light scattering by particles with complex morphologies.

The optical properties (or, electromagnetic/light-scattering characteristics) of small particles are fundamental to many disciplines including physics, astrophysics (e.g., the study of interstellar dust), planetary science (e.g., the explanation of the optical phenomena observed by a recent Mars lander), bio-optics, industry, ocean optics, atmospheric remote sensing (viewing the atmosphere and possibly the underlying land or ocean surface by satellites), and radiation parameterization in climate science (determining the climate effect of the buildup of greenhouse gases), to list just a few. The scattering of light by a sphere, now widely referred to as the Lorenz-Mie theory, was formulated more than 100 years ago by two eminent physicists, L. Lorenz (1890) and G. Mie (1908). However, stable and efficient programs for the Lorenz-Mie computations were developed in the 1970s and 1980s. In particular, Kattawar & Plass (1967) showed that a downward recurrence scheme was necessary to insure numerical stability of the computations involved in the Lorenz-Mie theory. With today's computational resources, it is now a trivial task to compute the optical properties of a sphere with a size between the Rayleigh regime (i.e., the particle size is much smaller than the wavelength of the incident electromagnetic wave) and the geometric optics regime (i.e., the particle size is much larger than the wavelength of the incident electromagnetic wave).

However, many particles (e.g., ice crystals in cirrus clouds and airborne dust aerosol particles) and living organisms (both terrestrial and aquatic) are nonspherical. Historically, these particles have been treated by using the so called "equivalent" sphere approximation. Unfortunately, the "equivalent" sphere approximation usually leads to significant errors and even misleading results in the calculated optical properties and downstream applications. Below we focus on high clouds (ice clouds) as a key example in this regard. Clouds with cloud-base heights above about 6 km are usually referred to as high clouds, including cirrus (Ci), cirrostratus (Cs), and cirrocumulus (Cc). The International Satellite Cloud Climatology Project (ISCCP) cloud classification scheme (Rossow & Schiffer 1999) defines clouds with cloud-top pressures less than 440 hPa (approximately higher than 6,500 m based on typical mid-latitude atmospheric profiles, https://www.weather.gov/epz/wxcalc_pressurealtitude) as high clouds including cirrus, cirrostratus, and deep convection. Figure 1 shows cirrus clouds that are delicate and wispy, observed in College Station, Texas, on September 24. 2023. In addition, three aviation-induced contrails (two linearly shaped and one in a curved shape) are shown in Fig. 1 (in the lower portion of the photo). A reader interested in the optical properties and climate impacts of contrails is referred to Yang et al. (2010) and Brasseur et al. (2016).

High clouds cover approximately 20% of the globe and 30% of the tropics (Liou & Yang 2016). For example, Fig. 2 shows the distributions of high cloud (ice cloud) fractions over the tropics (30°S-30°N) based on the observations made by the Moderate Resolution Imaging Spectroradiometer (MODIS) instruments (Salomonson et al. 1989; King et al. 1992) on Terra and Aqua satellites between 2002-2005 (Hong et al. 2007). The Terra satellite crosses the equator at 10:30am mean local time in a descending mode, while Aqua satellite crosses the equator at 01:30pm mean local time in an ascending mode. Therefore, the left and right panels in Fig. 2 show the high-cloud fraction distributions in the morning and afternoon, respectively. On average, the seasonal variation of the high cloud coverage over the tropics is approximately 25%-35%, mainly over the South Pacific convergence zone, the intertropical convergence zone, tropical Africa,

Figure 1. Cirrus clouds and contrails observed at 18:08 local time in College Station, Texas on September 24, 2023.

the Indian Ocean, and tropical and South America. If subvisible thin cirrus clouds are considered, ice cloud coverage over the Tropics would be more pronounced (Lee et al. 2009). For example, subvisible cirrus clouds 14.2-18.7 km above the surface with horizontal extents up to 2,700 km were observed by a lidar system mounted on a space shuttle (Winker & Trepte 1998). These thin cirrus clouds are essentially transparent for incoming solar radiation but strongly block outgoing longwave thermal emission from the lower atmosphere and the surface, warming the earth.

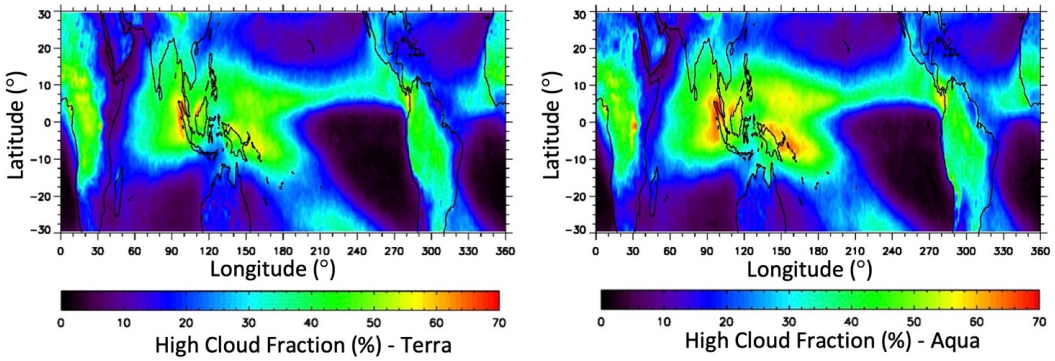

Figure 2. Geographical distribution of the three-year (2002-2005) mean high cloud fractions over the Tropics (30S-30N). Adopted from Hong et al. (2007) [© American Meteorological Society. Used with permission.]

Ice clouds are almost exclusively composed of nonspherical ice crystals with various shapes, including pristine hexagonal columns and plates, dendrites, bullet rosettes, and aggregates. Ice crystals with small-scale surface irregularities or surface roughness and inhomogeneous ice crystals with air bubbles included are common, as confirmed from in-situ observations. The optical properties of a particle are sensitive to the aforementioned small-scale irregularity at a wavelength where the particle is not absorptive. It has been demonstrated that particle surface roughness is a critical morphological factor in light scattering computation, which has important implications in remote sensing and radiative forcing assessment concerning ice clouds (Yang et al. 2008; Yi et al. 2013). Figure 3 shows some ice crystal habits (Bailey & Hallett 2009). As one can see, some of these particle morphologies are so complex that it is challenging to compute their optical properties accurately.

Before the early 1990s, atmospheric ice crystals were treated as spheres based on the "equivalent" spherical approximation in remote sensing and climate studies, because of lack of adequate light-scattering computational capabilities. Various studies (Liou & Yang 2016, and references cited therein) demonstrated that the aforementioned "equivalent" spherical approximation is inadequate for light-scattering computations and many practical applications. For example, Fig. 4 illustrates the impact of ice crystal nonsphericity on the simulation of

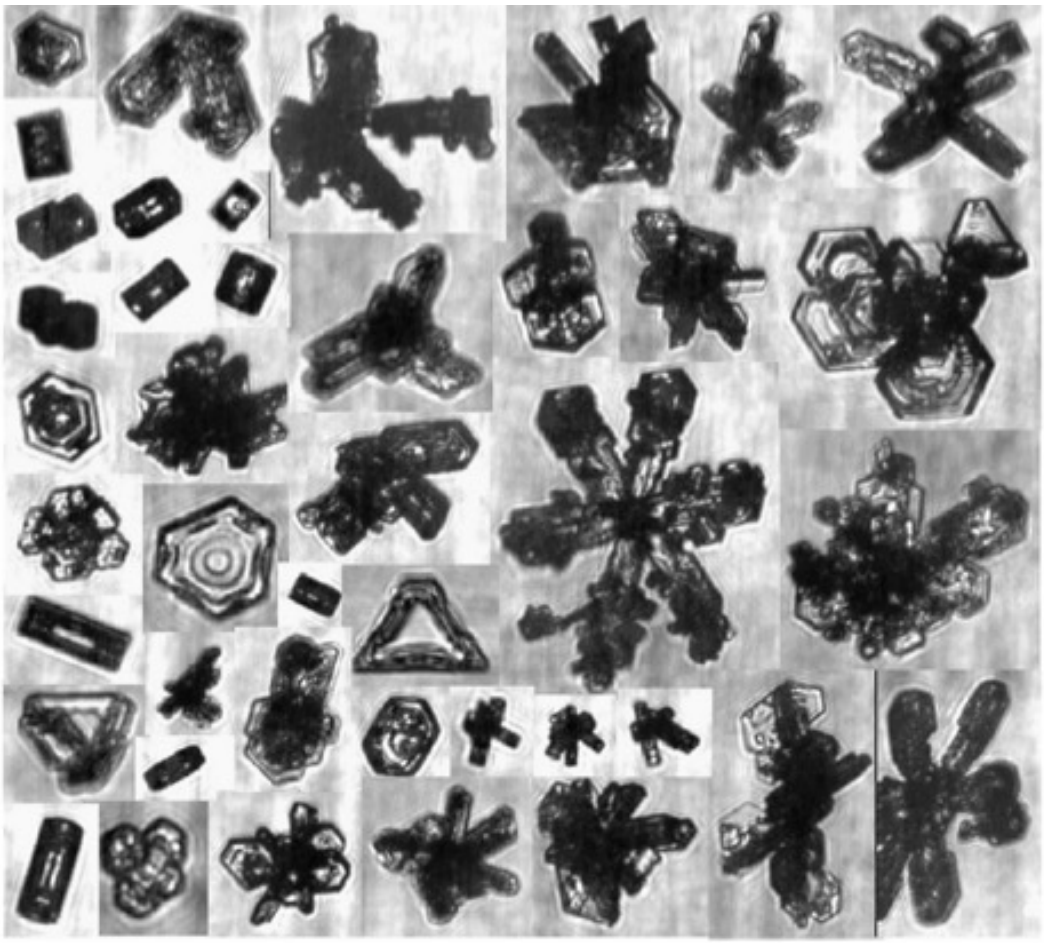

Figure 3. CPI (Lawson et al., 1998) images collected from the top of a convective tower over Lake Huron during the AIRS II field experiment. No visible overlying cirrus were present at the time, although lidar data might indicate the presence of subvisual cirrus at an altitude of 6–7 km. Crystals presented are to illustrate habit and are not on the same size scale. Adopted from Bailey and Hallett (2009) [© American Meteorological Society. Used with permission]. The permission for the use of this diagram was also granted by Prof. Matthew Bailey at the University of Nevada-Reno.

surface temperature using a climate model, the Community Earth System Model version 2 (CESM 2; Danabasoglu et al. 2020) for a 10-year period of monthly simulated climatology from 2005-2014. CESM2 simulations were configured with an active atmosphere with a satellite phenology land mode and prescribed ocean and sea ice modes. The model has 32 vertical atmospheric layers and horizontal resolution of 1.9 deg. (latitude) by 2.5 deg. (longitude). In particular, Fig. 4a shows the computed surface temperature (K) based on the “equivalent”

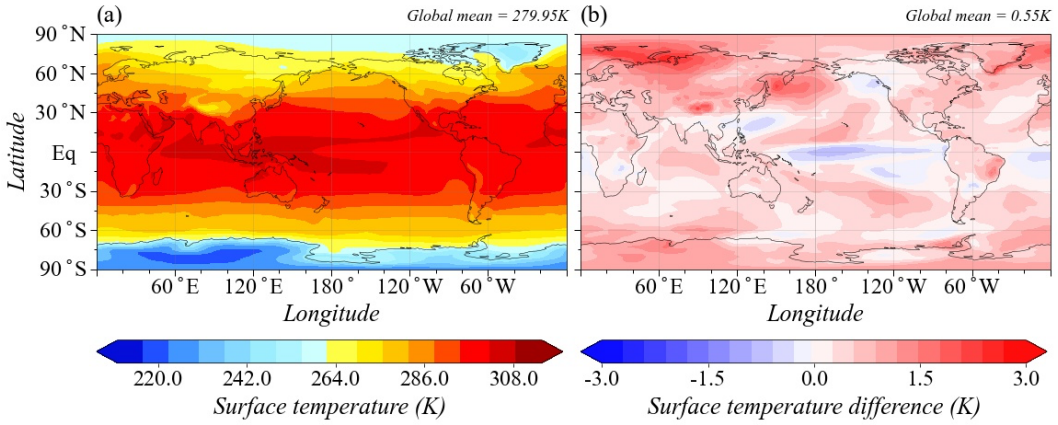

Figure 4. (a) 10-year averaged surface temperature (units: K) simulated with spherical ice cloud optical properties; (b) The error, or difference, in simulated surface temperature based on the spherical ice model minus surface temperature based on the THM. Note: The global area-averaged value is labeled at the upper right corner of each subplot.

spherical approximation for ice crystal habits. The global mean surface temperature is 279.95K. Figure 4b shows the difference of the derived temperatures based on "equivalent" spherical ice crystals minus those based on nonspherical ice crystals. The nonspherical ice crystal simulations are based on the two-habit model (THM) (Loeb et al. 2018). It is seen from Fig. 4b that the impact of ice crystal nonsphericity is pronounced and can be approximately 1K in many regions around the globe and even as large as 2K in some high-latitude regions. The global mean temperature difference between the spherical and nonspherical models is 0.55K. At present, the projections of future climate change are essentially dependent on climate models under different forcing scenarios (Eyring et al. 2016). The results shown in Fig. 4 present a convincing case that, to reduce the uncertainties in climate modeling, it is critical to realistically represent nonspherical ice crystals in climate studies.

Basics of Light Scattering by a Particle.–Figure 5 illustrates the geometric configuration for light scattering by a nonspherical particle. To compute the optical properties of the particle, it is necessary to decompose the electric vectors associated with the incident and scattered waves into two components perpendicular and parallel to the scattering plane which contains the incident and scattering directions.

The scattered electric vector components and their incident field counterparts can be linked through the amplitude scattering matrix in a symbolic form as:

$$\left[\begin{array}{cc} E_{\parallel}^{i} & E_{\perp}^{i} \end{array}\right]^{\dagger} \xrightarrow{S} \left[\begin{array}{cc} E_{\parallel}^{s} & E_{\perp}^{s} \end{array}\right]^{\dagger}, \tag{1a}$$

where the superscript $\dagger$ indicates the matrix transpose. The amplitude scattering matrix is a 2×2 matrix with complex elements in the form

$$S=\left[\begin{array}{cc} S_2 & S_3 \\ S_4 & S_1 \end{array}\right]. \tag{1b}$$

The elements of the amplitude scattering matrix depend on the scattering angle and the azimuthal angle of the scattering plane. Because every element of the amplitude scattering matrix is a complex quantity, having both an amplitude and a phase, this matrix contains eight pieces of independent information for a general nonspherical particle. Since only relative phase is important in scattering problems, it reduces the number of independent quantities to seven. In Eq. (1b), the ordering of the S matrix elements follows the extensively used convention (van de Hulst 1957). For three-dimensional scattering particles, analytical solutions based on the separation of variables method (SVM) are available for spheres (Lorenz 1890; Mie 1908) and spheroids (Asano & Yamamoto 1975). In the case of light scattering by a sphere, the amplitude scattering matrix is diagonal, and efficient programs have been developed to compute the elements S_1 and S_2 based on the analytical Lorenz-Mie formulas. However, it is still an active research area to numerically implement the SVM for spheroids for cases where large size parameters are needed, particularly for particles with large aspect ratios (the ratio of the maximum dimension to the minimum dimension of the particle).

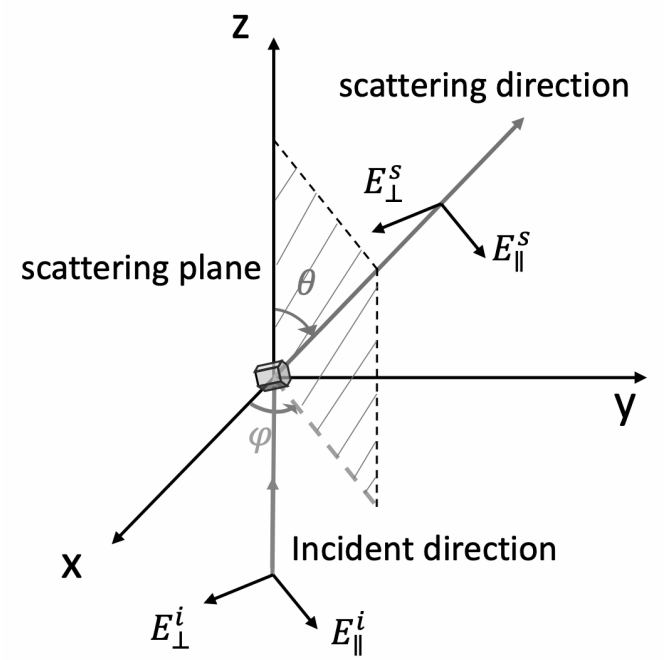

Figure 5. A schematic diagram illustrating the incident and scattering configuration for the scattering of light by a nonspherical particle.

Although the electric vector components are involved in Eq. (1), optical sensors do not measure electric and magnetic fields. Radiometric and polarimetric measurements by optical sensors are conducted with respect to Stokes parameters indicated by (I,Q,U,V) defined as

$$I = \frac{c}{8\pi}\left(E_{//}E_{//}^{*} + E_{\perp}E_{\perp}^{*} \right), \tag{2a}$$

$$Q = \frac{c}{8\pi}\left(E_{//}E_{//}^{*} - E_{\perp}E_{\perp}^{*} \right), \tag{2b}$$

$$U = \frac{c}{8\pi}\left(E_{//}E_{\perp}^{*} + E_{//}^{*}E_{\perp} \right), \tag{2c}$$

$$V = i\frac{c}{8\pi}\left(E_{//}E_{\perp}^{*} - E_{//}^{*}E_{\perp} \right), \tag{2d}$$

where the decomposition of the electric vector into the parallel and perpendicular components are with respect to a reference plane of

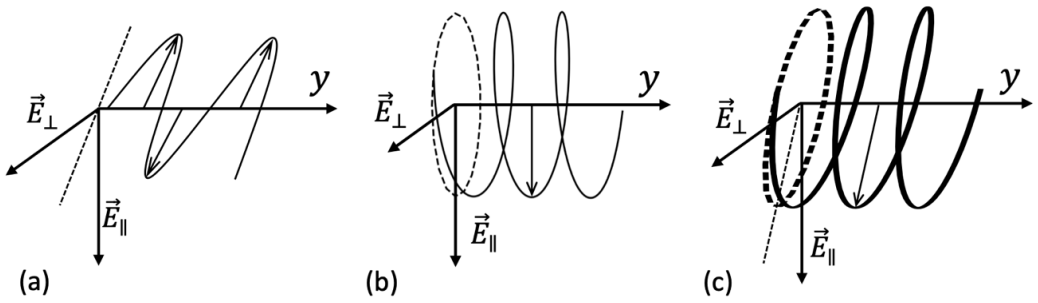

Figure 6. Illustrations of polarization, (a) linear, (b) circular, and (c) elliptic.

interest. In the above equations, *c* indicates the speed of light in vacuum. From the perspective of optical measurement, two light beams with the same Stokes parameters are indistinguishable (Chandrasekhar 1960). An electromagnetic wave is a vector wave. To specify it, both the wave amplitude and the polarization state are required. The polarization indicates the form of the electric vector oscillations. In Fig. 6, panels (a), (b) and (c) illustrate linear, circular, and elliptical polarization configurations, respectively, where the projections of the electric vector on a plane perpendicular to the wave propagation direction are a straight line (panel a), circle (panel b), and ellipse (panel c) denoted by the dashed line and curves.

The polarization state of a light beam can be fully described by the Stokes parameters. In particular, the first Stokes parameter *I* indicates the intensity of the beam, which is what is perceivable for the human eye. Q and U specify linear polarization, and V is associated with circular polarization. Figure 7 schematically illustrates the polarization states in conjunction with various combinations of the Stokes parameters with the propagation of the light beam toward the observer. The circular polarization configurations in the upper right and lower right panels are referred to as right and left circular polarization, respectively. However, opposite definitions of right and left circular polarization can be found in the literature, for which the propagation of the beam is away from the observer. The history of the two different definitions can be found in Bohren & Huffman (1983).

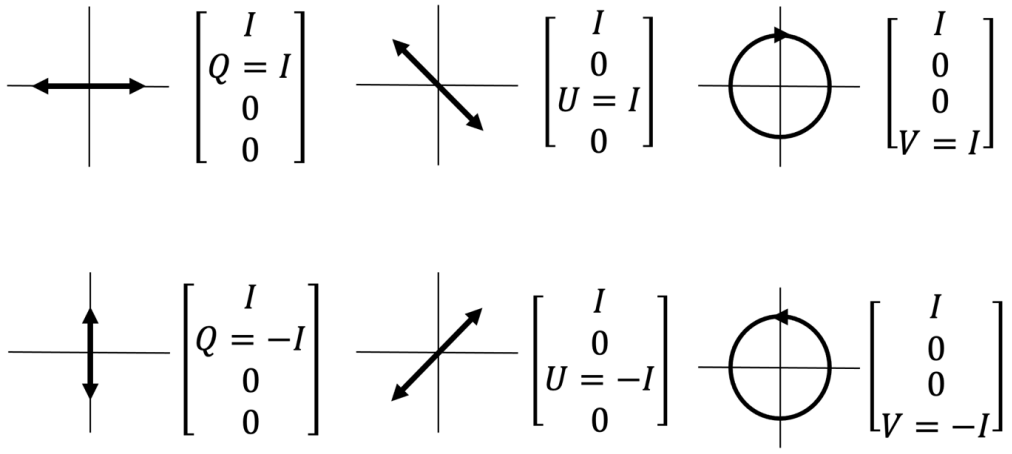

Figure 7. Polarization configurations for linearly polarized light (left and middle columns) and circular polarized light (right column). Note that the light propagation direction points out of the paper (i.e., the observer looks towards the light source). The upper-right diagram illustrates right circular polarization, and the lower-right diagram illustrates left circular polarization.

Without going through a detailed mathematical derivation, we can use Eq. (1) to obtain the relation linking the incident and scattered Stokes parameters in the form

$$\begin{bmatrix} I_i & Q_i & U_i & V_i \end{bmatrix}^{\dagger} \xrightarrow{\sigma_s P} \begin{bmatrix} I_s & Q_s & U_s & V_s \end{bmatrix}^{\dagger}, \tag{3a}$$

$$P = \begin{bmatrix} P_{11} & P_{12} & P_{13} & P_{14} \\ P_{21} & P_{22} & P_{23} & P_{24} \\ P_{31} & P_{32} & P_{33} & P_{34} \\ P_{41} & P_{42} & P_{43} & P_{44} \end{bmatrix}, \tag{3b}$$

where σ_s is referred to as the scattering cross section, a quantity indicating the ability of the particle to redistribute the incident energy into other directions in the 4π steradian space. The 4×4 P matrix is referred to as the phase matrix. Ice crystals in the atmosphere are usually randomly oriented. However, when the atmosphere is very stable, ice crystals with the geometries of plates and columns have preferred orientations. Under the condition that ice crystals are

randomly oriented with an equal number of mirror-imaging positions, the phase matrix reduces to a block-diagonal form with six independent elements (van de Hulst 1957). The phase matrix element P_{11}, called the phase function, is especially interesting to many applications, as it specifies the angular distribution of scattered light, from 0° (pure forward scattering or no deviation from the emitted direction) to 180° (pure backscattering or scattering exactly in the opposite direction of the incident light). As an example, Figure 8 shows the phase functions of an ensemble of water droplets assumed to be spherical and a hexagonal ice crystal under the random orientation condition. In the left panel with the sun as the light source, the two peaks corresponding to the primary and secondary rainbows are indicated in the sky opposite the sun (scattering angles near 140°). The low-value region of the phase function between the two rainbow peaks corresponds to the Alexander dark band. Note that the phase function of an individual sphere usually displays fluctuations. Shown in the left panel is the phase function of an ensemble of spheres, such as raindrops. <D>, referred to as the effective particle diameter, indicates an ensemble-average quantity. In the right panel, the two scattering peaks correspond to 22° and 46° halos (22° and 46° from the sun). The reader is referred to Greenler (1980) and Tape & Moilanen (2006) for the detailed explanations of the physical processes of rainbows and halos.

For a sphere or an ensemble of randomly oriented particles, the phase function is one-dimensional, depending only on the scattering angle. For a nonspherical ice crystal with a specific orientation, the phase function depends on both the scattering angle (0° to 180°) and the azimuthal angle of the scattering plane (-180° to 180°). As an example, the left panels in Fig. 9 show the phase functions of horizontally oriented hexagonal ice plates and columns. Obviously, these phase functions display complex angular features (distorted by mapping the observer's angular view onto a linear two-dimensional grid) that lead to fascinating optical phenomena. The right panels show the optical phenomena caused by a mixture of randomly and horizontally oriented ice particles (the upper right simulates a wide-angle view, and the lower right simulates a "fish-eye" view of the entire sky). It is worth pointing out the two bright spots on each side of the

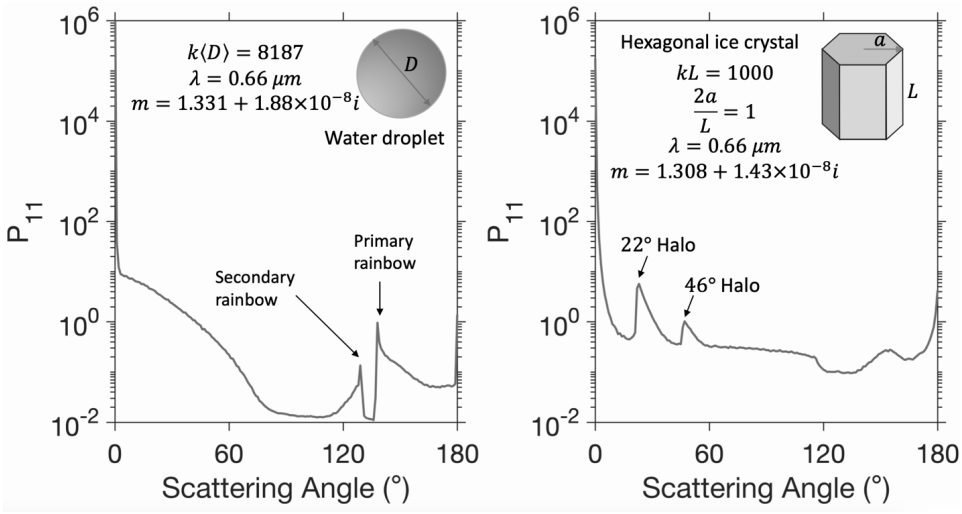

Figure 8. (Left) the phase function of a water droplet; (Right) the phase function of a hexagonal ice crystal under the random orientation condition.

sun in the upper right panel of Fig. 9 are called sundogs, which are caused by horizontally oriented hexagonal plates when the elevation of the sun in the sky is low. For detailed explanations of the physical processes of all the optical phenomena associated with ice crystals, the reader is referred to Greenler (1980), Tape & Moilanen (2006) and Liou & Yang (2016).

Synergistically Unified Method for Light-Scattering Computations.–To compute the optical properties of a large nonspherical ice crystal much larger than the incident wavelength, the only feasible method is the geometric optics method. The left panel in Fig. 10 schematically illustrates the conventional geometric optics method (Wendling et al. 1979; Cai & Liou 1982). Specifically, the incident wave is approximated as a bundle of rays. The principles of geometric optics can be used to compute the electric field associated with reflected and transmitted rays using the ray-tracing technique through simulating a large number of rays. In addition to the contribution by the rays, diffraction also contributes to the scattering of incident light. In the conventional geometric optics method, the diffraction contribution is approximately considered based on the Fraunhofer diffraction theory (Born & Wolf 1970). This method suffers

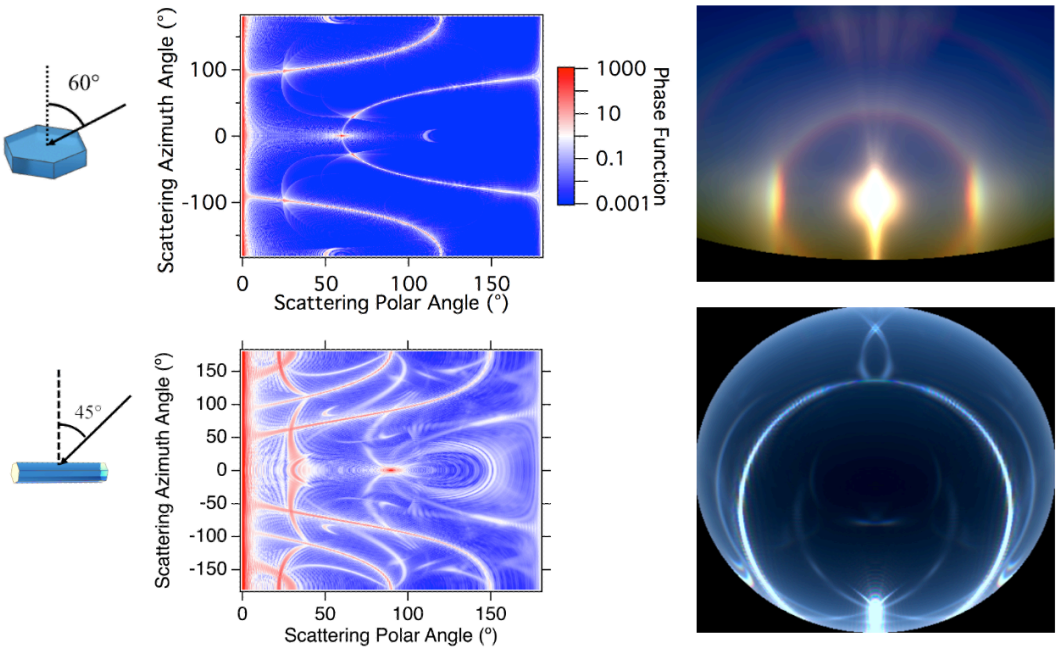

Figure 9. (Far left diagrams) Two examples of horizontally oriented atmospheric ice crystal types, (upper left) thin hexagonal plates illuminated by sunlight with the sun 60° from the vertical, and (lower left) long hexagonal columns with the sun 45° from the vertical. For a population of ice crystals with a mixture of sizes and random rotations around the zenith (dotted or dashed line), the panels in that row show corresponding optical properties. (Left panels) 2D phase function of the mixture of horizontally oriented ice crystals; (right panels) simulated sky view of the optical phenomena associated with that mixture. The upper right simulates a wide-angle view, and the lower right simulates a "fish-eye" view of the entire sky. The optical property data are from Saito and Yang (2019). Diagrams are adopted from Yang et al. (2018) [the reuse of these diagrams are permitted under the open access Creative Common CC BY license].

from some significant shortcomings. For example, the extinction efficiency (the ratio of the cross section attenuating the incident light to the projected area of the particle) Q_e is assumed to be a constant, i.e., $Q_e = 2$. The phase function has singularities in the forward and backward directions. At a visible wavelength where ice has very little absorption, the ray-tracing contribution to the phase function based on the conventional geometric optics method is unphysically independent of the particle size.

The physical-geometric optics method (PGOM) illustrated in the right panel of Fig. 10 is developed to overcome the inherent

shortcomings of the conventional geometric optics method. In PGOM, the diffraction and ray-tracing components are not artificially separated. The ray-tracing technique is utilized to compute the electric and magnetic fields on the particle surface. The near field thus obtained is subsequently mapped to the far field (in the zone far away from the particle, or the radiation zone) based on an exact electromagnetic relation to compute the optical properties of the particle. We have demonstrated that PGOM is much more accurate than the conventional geometric optics method. For the first time, the principles of geometric optics are utilized in PGOM to simulate the particle extinction efficiency that is dependent on the particle size. Furthermore, PGOM is applicable to a much wider particle size range, compared to its conventional counterpart. The PGOM concept was developed in the 1990s based on a surface-mapping technique (Yang & Liou 1996) and a volume-mapping technique (Yang & Liou 1997). However, computationally efficient PGOM programs were developed through our persistent efforts (Bi et al. 2011; Sun et al. 2017; Yang et al. 2019) at Texas A&M University by leveraging advanced computing techniques including computer graphics techniques. To the best of our knowledge, at present PGOM is the most appropriate method for computing the optical properties of nonspherical particles with moderate-to-large sizes as compared to the wavelength of the incident light.

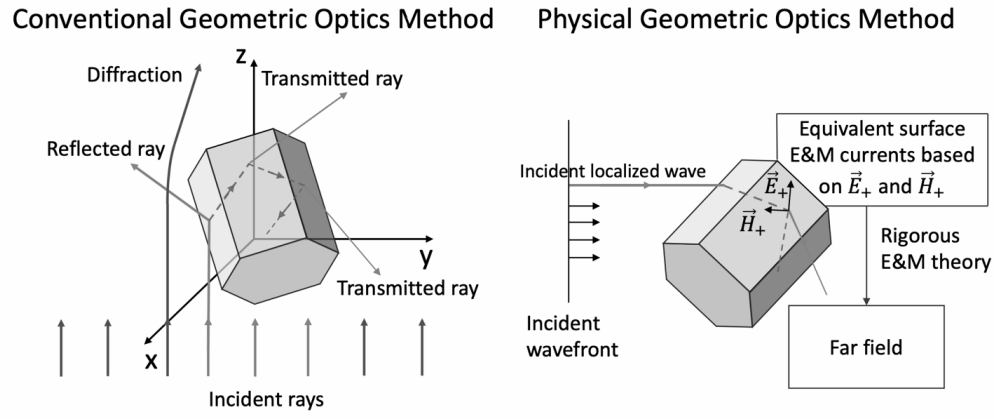

Figure 10. Schematic diagrams for the conventional geometric optics method (CGOM; left panel), and the physical geometric optics method (PGOM; right panel).

For nonspherical particles with small-to-moderate sizes compared to the wavelength of the incident light, we can use the T-matrix method. In this method, the incident and the scattered fields are expanded using vector spherical wave functions (VSWFs) as follows (Waterman 1971; Tsang et al. 2000; Mishchenko et al. 2002):

$$\mathbf{E}^{\mathrm{inc}}(\vec{r}) = \sum_{n=1}^{\infty} \sum_{m=-n}^{n} a_{mn} \mathrm{Rg}\mathbf{M}_{nm}(k\vec{r}) + b_{mn} \mathrm{Rg}\mathbf{N}_{nm}(k\vec{r}), \tag{4a}$$

$$\mathbf{E}^{\mathrm{sca}}(\vec{r}) = \sum_{n=1}^{\infty} \sum_{m=-n}^{n} p_{mn} \mathbf{M}_{nm}(k\vec{r}) + q_{mn} \mathbf{N}_{nm}(k\vec{r}), \quad r > r_{\mathrm{c}}, \tag{4b}$$

The expansion coefficients in the above equations can be linked through the T-matrix in the form

$$\left[p_1, q_1 \cdots p_{l_{\max}}, q_{l_{\max}}\right]^{\dagger} = T\left[a_1, b_1 \cdots a_{l_{\max}}, b_{l_{\max}}\right]^{\dagger}, \tag{5a}$$

where the superscript $\dagger$ indicates the matrix transpose. The T-matrix T is given by

$$\mathbf{T} = \begin{bmatrix} \mathrm{T}_{11}^{11} & \mathrm{T}_{11}^{12} & \cdots & \cdots & \mathrm{T}^{11}_{1,l_{\max}} & \mathrm{T}^{12}_{1,l_{\max}} \\ \mathrm{T}_{11}^{21} & \mathrm{T}_{11}^{22} & \cdots & \cdots & \mathrm{T}^{21}_{1,l_{\max}} & \mathrm{T}^{22}_{1,l_{\max}} \\ \cdots & \cdots & \cdots & \cdots & \cdots & \cdots \\ \cdots & \cdots & \cdots & \cdots & \cdots & \cdots \\ \mathrm{T}^{11}_{l_{\max},1} & \mathrm{T}^{12}_{l_{\max},1} & \cdots & \cdots & \mathrm{T}^{11}_{l_{\max},l_{\max}} & \mathrm{T}^{12}_{l_{\max},l_{\max}} \\ \mathrm{T}^{21}_{l_{\max},1} & \mathrm{T}^{22}_{l_{\max},1} & \cdots & \cdots & \mathrm{T}^{21}_{l_{\max},l_{\max}} & \mathrm{T}^{22}_{l_{\max},l_{\max}} \end{bmatrix}. \tag{5b}$$

The T-matrix is an inherent physical property of the scattering particle and is independent of the incident wave. This unique quality allows us to obtain the mean optical properties averaged over random orientations (Mishchenko 1991; Mishchenko et al. 2002) in an analytical form. For example, the scattering cross section is given by

$$\langle \sigma_{sca} \rangle = \frac{2\pi}{k^2} \sum_{l=1}^{l_{\max}} \sum_{l'=1}^{l_{\max}} \left(\left| T_{ll'}^{11} \right|^2 + \left| T_{ll'}^{12} \right|^2 + \left| T_{ll'}^{21} \right|^2 + \left| T_{ll'}^{22} \right|^2 \right) . \qquad (6)$$

The T-matrix is conventionally implemented by using a surface-integration based technique referred to as the extended boundary condition method (EBCM) (Waterman 1971; Tsang et al. 2000; Mishchenko et al. 2002). EBCM is limited to relatively regular particle geometries such as spheroids and circular cylinders. The numerical stability of EBCM encounters significant challenges for moderate particle sizes with large aspect ratios.

Johnson (1988) demonstrated that the T-matrix method can be implemented via a volume-integration technique, referred to as the invariant imbedding T-matrix method (IITM), and showed numerical results for small spheroids. However, this paper was buried in the literature; in particular, when we noticed this paper in 2011, there were only several citations of Johnson (1988). Our research group made a quantum-leap contribution to the IITM theory and effectively implemented it for arbitrarily shaped particles (Bi et al. 2013a,b; Bi & Yang 2014; Sun et al. 2020; Yang et al. 2019). We have extensively validated our implementation of the IITM method by comparing the IITM simulations with the EBCM results in the case of spheroids and with the results based on other numerical methods for complex geometries.

Figure 11 illustrates the principle of the IITM. In particular, a particle can be viewed as being composed of an inhomogeneous sphere with many layers. Each spherical layer defined in this form can be inhomogeneous, that is, portions of the layer can be empty. If we know the T-matrix for a core (from layer 1 to n-1) of the above inhomogeneous sphere, whose T-matrix is denoted as $\mathbf{T}(r_{n-1})$, we can conduct various volume-integration based matrix operations to obtain

$$\mathbf{T}(r_{n-1}) \xrightarrow{\text{volume integration based matrix operations}} \mathbf{T}(r_n), \qquad (17)$$

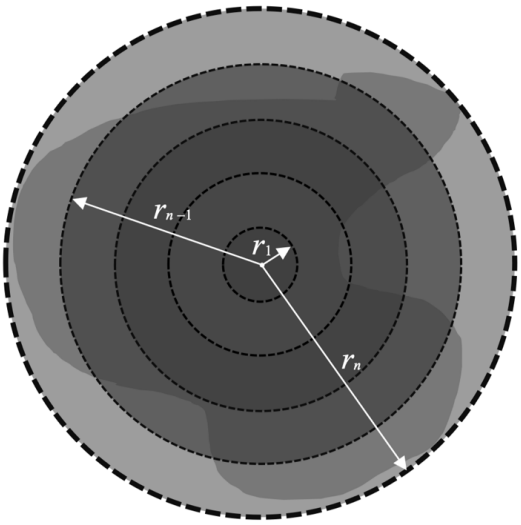

Figure 11. Schematic illustration of the invariant-imbedding T-matrix method for light scattering computation.

$\mathbf{T}(r_n)$ for a larger core by adding the nth layer. In this manner, we can compute the T-matrix of the entire particle via an iterative approach.

As an example, Fig. 12 shows the phase function P_{11} and $-P_{12}/P_{11}$ [this quantity indicates the degree of linear polarization of scattered light if the incident light is unpolarized (Hovenier et al. 2004)] for a randomly oriented hexagonal ice crystal with size parameter kL=200 and aspect ratio a/L=1. In our previous study (Yang et al. 2019), we applied IITM to ice crystals as large as kL=300. To the best of our knowledge, at present IITM is the only numerically accurate method that is applicable to such large nonspherical ice particles, particularly under the random orientation condition. We also show the PGOM results in Fig. 12. Although PGOM is an approximate method, the PGOM results are very close to the IITM benchmark.

The accuracy of PGOM increases with increasing particle size because this method is partially based on the principles of geometric optics. IITM is a theoretically exact method except for very small errors in numerical computation. However, IITM requires more computational resources with increasing particle size and becomes

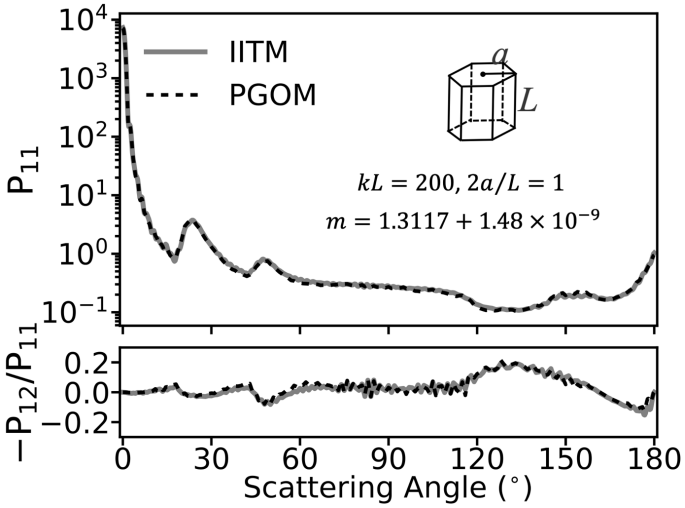

Figure 12. Phase function P_{11} and $-{}^{P_{12}}/_{P_{11}}$ computed by IITM and PGOM for a hexagonal column.

unfeasible for large particles. Figure 12 shows the extinction efficiency computed by the IITM and PGOM. Between kL=100 and 200, the two results overlap. The smooth transition between the IITM and PGOM leads to the concept of the synergistically unified method. Specifically, we can use the IITM for kL<100 and PGOM for larger particles, as illustrated by the lower panel in Fig. 13. In our opinion, the synergistically unified method represents a breakthrough in light-scattering computation, as it provides a practical approach to solving the optical properties for many applications.

The applications of the synergistically unified method for light-scattering computations are not limited to the study of ice clouds. As an example, we use the computational capabilities to simulate the optical properties of nonspherical dust aerosols and applied the results to explain the polarimetric observation of a dust storm over the Red Sea on 6/27/2007 (upper panel of Fig. 14) made by a polarimeter on a French satellite. The lower panel compares the observation and simulations based on the "equivalent" spherical approximation and nonspherical particles. Obviously, the comparison indicates that dust particles are nonspherical. This finding is consistent with various in situ and laboratory measurements of dust particle shapes (e.g., Muñoz 2012).

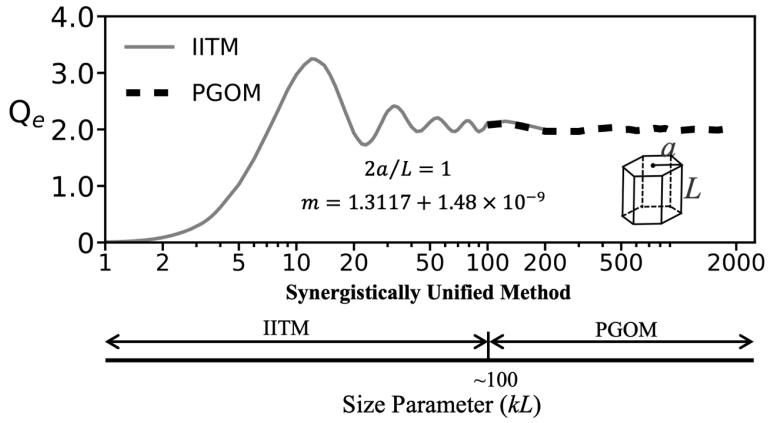

Figure 13. (upper panel) Comparison of the extinction efficiencies computed by the IITM and PGOM; (lower panel) illustration of the synergistically unified method based on combining IITM and PGOM for light-scattering computation.

Summary.–In the past twenty years, the two authors have been collaborating on various research fronts and trained a number of outstanding graduate students and postdoctoral researchers. A key example of their accomplishments is research and development of state-of-the-art light-scattering computational capabilities, particularly, the synergistically unified method based on combining the invariant-imbedding method and the physical geometric optics method to compute the optical properties of nonspherical particles over the entire natural size range.

The properties computed using these advanced capabilities have profound impacts on many applications. To list a few, the ice crystal optical properties we developed are essential for the satellite-based operational ice cloud property retrieval products developed respectively by the Moderate Resolution Imaging Spectroradiometer (MODIS) Science Team at NASA Goddard Space Flight Center (Platnick et al. 2017), the CALIPSO Imaging Infrared Radiometer (IIR) Science Team (Garnier et al. 2013) and the Clouds and the Earth's Radiant Energy System (CERES) Science Team at NASA Langley Research Center (Minnis et al. 2021), and the Atmospheric Infrared Sounder (AIS) Science Team at NASA Jet Propulsion Laboratory (Kahn et al. 2014. Note: the optical properties reported in Baum et al. 2007 were used). Our ice cloud property data is incorporated into the

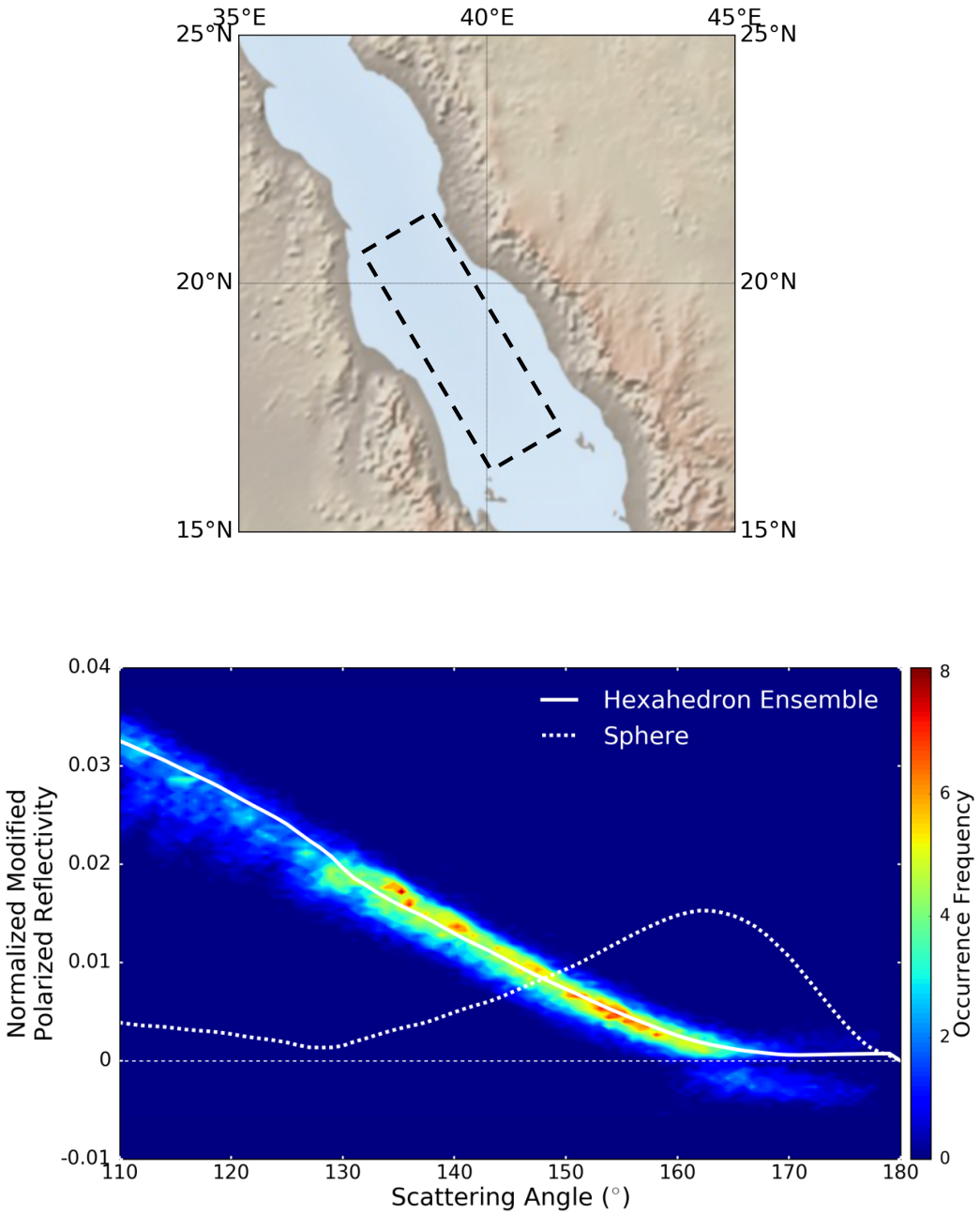

Figure 14. Observed and simulated normalized modified polarized reflectivity (L_{nmp}) from dust aerosols over the Red Sea. The upper panel is the location of the dust aerosol observation. The data from the dashed rectangle area in the upper panel is shown in the lower panel. The lower panel shows the observed and simulated L_{nmp} at wavelength 0.865 nm. The color contour indicates pixel-level observations. The white solid line is the simulation assuming a hexahedron ensemble model of dust aerosols. The white dashed line is the simulation assuming spheres as the dust aerosol shape [adapted from Yang et al. (2019), reproduced courtesy of The Electromagnetic Academy].

widely used radiative transfer packages such as libRadtran developed by German scientists (see "LibRadtran User's Guide" by Mayer & Kylling 2005), and the Community Radiative Transfer Model (CRTM) (Liu & Lu 2016) that is a flagship effort of the NOAA Joint Center for Satellite Data Assimilation (JCSDA) to facilitate forward radiative transfer simulations in satellite remote sensing implementations. Our optical property datasets are also used in radiative parameterizations (Fan et al. 2023) in an offline version of the E3SM climate model developed by the U.S. Department of Energy (DOE).

We wish to point out that the light-scattering computational capabilities we developed find applications beyond geoscience remote sensing. For example, IITM has been applied to bio-optics, particularly the study of the optical properties of red blood cells (Bi & Yang 2013). Our light-scattering computational models also find applications in astrophysics (in particular, study of interstellar dust, Ding et al. 2021), the explanation of the optical phenomena observed by a Mars rover (Ding et al. 2023), and ocean optics (Wei et al. 2021).

ACKNOWLEDGMENTS

The authors are grateful for the help with computations and illustrations provided by Jian Wei (Fig. 4), Yuheng Zhang (Figs. 5, 7, 8, and 10 with Dongchen Li), and Jiachen Ding (Figs. 6, 11, 12, and 13). Dr. Steven Schroeder edited the manuscript.

LITERATURE CITED

Asano, S. & G. Yamamoto. 1975. Light scattering by a spheroid particle. Appl. Opt. 14:29-40.

Bailey, M. P. & J. Hallett. 2009. A comprehensive habit diagram for atmospheric ice crystals: Confirmation from the laboratory, AIRS II, and other field studies. J. Atmos. Sci. 66(9):2888-2899. DOI 10.1175/2009JAS2883.1.

Baum, B. A., P. Yang, S. L. Nasiri, A. K. Heidinger, A. J. Heymsfield & J. Li. 2007. Bulk scattering properties for the remote sensing of ice clouds. Part III: High-resolution spectral models from 100 to 3250 cm^{-1}. J. Appl. Meteorol. Climatol. 46:423–434.

Bi, L. & P. Yang. 2014. Accurate simulation of the optical properties of atmospheric ice crystals with the invariant imbedding T-matrix method. J. Quant. Spectrosc. Radiat. Transf. 138:17–35.

Bi, L., P. Yang, G. W. Kattawar, Y. Hu & B. A. Baum. 2011. Scattering and absorption of light by ice particles: Solution by a new physical-geometric optics hybrid method. J. Quant. Spectrosc. Radiat. Transfer. 112:1492-1508. DOI 10.1016/j.jqsrt.2011.02.015.

Bi, L., P. Yang, G. W. Kattawar & M. I. Mishchenko. 2013a. Efficient implementation of the invariant imbedding T-matrix method and the separation of variables method applied to large nonspherical inhomogeneous particles. J. Quant. Spectrosc. Radiat. Transf. 116:169–183.

Bi, L., P. Yang, G. W. Kattawar & M. I. Mishchenko. 2013b. A numerical combination of extended boundary condition method and invariant imbedding method applied to light scattering by large spheroids and cylinders. J. Quant. Spectrosc. Radiat. Transf. 123(4):17–22.

Bi, L. & P. Yang. 2013. Modeling of light scattering by biconcave and deformed red blood cells with the invariant imbedding T-matrix method. J. Biomedical Optics 18(5): 055001-1 -- 055001-13.

Bohren, C. F. & D. R. Huffman. 1983. *Absorption and Scattering of Light by Small Particles*, New York, John Wiley and Sons.

Born, M. & E. Wolf. 1970: *Principles of Optics, 4th ed*. Paris, Pergamon Press.

Brasseur, G. P., M. Gupta, B. E. Anderson, S. Balasubramanian, S. Barrett, D. Duda, G. Fleming, P. M. Forster, J. Fuglestvedt, A. Gettelman, R. N. Halthore, S. D. Jacob, M. Z. Jacobson, A. Khodayari, K.-N. Liou, M. T. Lund, R. C. Miake-Lye, P. Minnis, S. Olsen, J. E. Penner, R. Prinn, U. Schumann, H. B. Selkirk, A. Sokolov, N. Unger, P. Wolfe, H.-W. Wong, D. W. Wuebbles, B. Yi, P. Yang & C. Zhou. 2016. Impact of aviation on climate: FAA's Aviation Climate Change Research Initiative (ACCRI) Phase II. Bull. Am. Meteorol. Soc. 97:561-583.

Cai, Q. & K. N. Liou. 1982. Polarized light scattering by hexagonal ice crystals: theory. *Appl. Opt.* 21:3569–3580.

Chandrasekhar, S. 1960. *Radiative Transfer*, London, Oxford Univ. Press.

Danabasoglu, G., J.-F. Lamarque, J. Bacmeister, D. A. Bailey, A. K. DuVivier, J . Edwards, L. K. Emmons, J. Fasullo, R. Garcia, A. Gettelman, C. Hannay, M. M. Holland, W. G. Large, P. H. Lauritzen, D. M. Lawrence, J. T. M. Lenaerts, K. Lindsay, W. H. Lipscomb, M. J. Mills, R. Neale, K. W. Oleson, B. Otto-Bliesner, A. S. Phillips, W. Sacks, S. Tilmes, L. van Kampenhout, M. Vertenstein1, A. Bertini, J. Dennis, C. Deser, C. Fischer, B. Fox-Kemper, J. E. Kay, D. Kinnison, P. J. Kushner, V. E. Larson, M. C. Long, S. Mickelson,J. K. Moore, E. Nienhouse, L. Polvani, P. J. Rasch & W. G. Strand. 2020. The Community Earth System Model Version 2 (CESM2). J. Adv. Model. Earth Systems. 12(2):1–35. https://doi.org/10.1029/2019MS001916

Ding, J., P. Yang, M. T. Lemmon & Y. Zhang. 2023. Simulations of halos produced by carbon dioxide ice crystals in the Martian atmosphere. Geophys. Res. Letters. 50: e2023GL103457. https://doi.org/10.1029/2023GL103457

Ding, J., L. Wang, P. Brown & P. Yang. 2021. Radiative transfer modeling of an SN 1987A Light Echo – AT 2019xis. Astrophys. J. 919:104 https://doi.org/10.3847/1538-4357/ac1069

Eyring, V., S. Bony, G. A. Meehl,, C. A. Senior, B. Stevens, R. J. Stouffer & K. E. Taylor. 2016. Overview of the Coupled Model Intercomparison Project Phase 6 (CMIP6)

experimental design and organization. Geosci. Model Dev. *9*(5):1937-1958. https://doi.org/10.5194/gmd-9-1937-2016

Fan, C., Y.-H. Chen, X. Chen, W. Lin, P. Yang & X. Huang. 2023. A refined understanding of the ice cloud longwave scattering effects in climate model. J. Adv. Model. Earth Systems.

Garnier, A., J. Pelon, P. Dubuisson, P. Yang, M. Faivre, O. Chomette, N. Pascal, P. Lucker & T. Murray. 2013. Retrieval of cloud properties using CALIPSO Imaging Infrared Radiometer. Part II: Effective diameter and ice water path. J. Appl. Meteor. Clim. 52:2582-2599.

Greenler, R., 1980: *Rainbows, Halos, and Glories*. New York, Cambridge University Press.

Hong, G., P. Yang, B.-C. Gao, B. A. Baum, Y. X. Hu, M. D. King & S. Platnick. 2007. High cloud properties from three years of MODIS Terra and Aqua Data over the Tropics. J. Appl. Meteor. Clim. 46:1840-1856.

Hovenier, J. W., C. Van Dee Mee & H. Domke. 2004. *Transfer of Polarized Light in Planetary Atmosphere*. Dordrecht, Netherlands, Kluwer Academic Publishers.

Johnson, B. R. 1988. Invariant imbedding T matrix approach to electromagnetic scattering, Appl. Opt. 27(23):4861.

Kahn, B. H., F. W. Irion, V. T. Dang, E. M. Manning, S. L. Nasiri, C. M. Naud, J. M. Blaisdell, M. M. Schreier, Q. Yue, K. W. Bowman, E. J. Fetzer, G. C. Hulley, K. N. Liou, D. Lubin, S. C. Ou, J. Susskind, Y. Takano, B. Tian & J. R. Worden. 2014. The Atmospheric Infrared Sounder version 6 cloud products2014: The Atmospheric Infrared Sounder version 6 cloud products. Atmos. Chem. Phys. 14:399–426.

Kattawar, G. W. & G. N. Plass. 1967. Electromagnetic scattering from absorbing spheres, Appl. Opt. 6:1377-1382.

King, M. D., Y. J. Kaufman, W. P. Menzel & D. Tanré. 1992. Remote sensing of cloud, aerosol, and water vapor properties from the Moderate Resolution Imaging Spectrometer (MODIS), IEEE Trans. Geosci. Remote Sens.30(1):2–27.

Lawson, R. P., A. V. Korolev, S. G. Cober, T. Huang, J. W. Strapp & G. A. Isaac. 1998. Improved measurements of the droplet size distribution of a freezing drizzle event. *Atmos. Res.* 47:81–191.

Lee, J, P. Yang, A. Dessler, B.-C. Gao & S. Platnick. 2009. Distribution and radiative forcing of tropical thin cirrus clouds. J. Atmos. Sci. 66:3721-3731.

Liou, K. N. & P. Yang. 2016. Light Scattering by Ice Crystals: Fundamentals and Applications, Cambridge University Press, ISBN 9780521889162, pp 443.

Liu, Q. & C.-H. Lu. 2016. Community radiative transfer model for air quality studies, in "Light Scattering Reviews", Vol. 11, 67-115, Springer Praxis Books, DOI 10.1007/978-3-662-49538-4_2

Loeb, N. G., P. Yang, F. G. Rose, G. Hong, S. Sun-Mack, P. Minnis, S. Kato, S.-H Ham, W. L. Smith Jr., S. Hioki & G. Tang. 2018. Impact of ice microphysics on satellite cloud retrievals and broadband flux radiative transfer model calculations. J. Climate. 31:1851-1864.

Lorenz, L. 1890. Lysbevegelser i og uden for en af plane Lysbolger belyst Kugle. *Det kongelig danske Videnskabernes Selskabs Skrifter, Naturvidenskab. Math. Afd.*, VI (1): 2–62.

Mayer, B. & Kylling, A. 2005. Technical note: The libRadtran software package for radiative transfer calculations - Description and examples of use. Atmos. Chem. Phys. 5:1855–1877. https://doi.org/10.5194/acp-5-1855-2005.

Mie, G. 1908. Beiträge zur Optik trüber Medien, speziell kolloidaler Metallösungen, *Annalen der Physik, Vierte Folge* 25:377–445.

Minnis, P., S. Sun-Mack, Y. Chen, F.-L.Chang, C. R. Yost, W. L. Smith, P. W. Heck, R. F. Arduini, S. T. Bedka, Y.Yi, G. Hong, Z. Jin, D. Painemal, R. Palikonda, B. R. Scarino, D. A. Spangenberg, R. A. Smith, Q. Z. Trepte, P. Yang & Y. Xie. 2021. CERES MODIS cloud product retrievals for Edition 4--Part I: Algorithm changes. IEEE Trans. Geosci. Remote Sens. 59:2744-2780. DOI 10.1109/TGRS.2020.3008866.

Mishchenko, M. I. 1991. Light scattering by randomly oriented axially symmetric particles. J. Optical Soc. America A 8:871-882.

Mischenko, M., L. Travis & A. Lacis, 2002. *Scattering, Absorption, and Emission of Light by Small Particles*. Cambridge University Press.

Muñoz, O., F. Moreno, D. Guirado, D. D. Dabrowska, H. Volten & J. W. Hovenier. 2012. The Amsterdam-Granada Light Scattering Database. J. Quant. Spectro. and Radiat. Transfer 113:566–574.

Platnick, S., K. G. Meyer, M. D. King, G. Wind, N. Amarashinghe, B. Marchant, G. T. Arnold, Z. Zhang, P. A. Hubanks, R. E. Holz, P. Yang, W. L. Ridgeway & J. Riedi. 2017. The MODIS cloud optical and microphysical products: Collection 6 updates and examples from Terra and Aqua, IEEE Trans. Geosci. Remote Sens. 55:502–525. DOI 10.1109/TGRS.2016.2610522.

Rossow, W. B. & R. A. Schiffer. 1999. Advances in Understanding Clouds from ISCCP, Bull. Amer. Meteor. Soc. 80:2261-2287.

Saito, M. & P. Yang. 2019. Oriented ice crystals: A single-scattering property database for applications to lidar and optical phenomenon simulations. J. Atmos. Sci. 76:2635-2652.

Salomonson, V. V., W. Barnes, P. W. Maymon, H. E. Montgomery & H. Ostrow. 1989. MODIS: Advanced facility instrument for studies of the Earth as a system. IEEE Trans. Geosci. Remote Sens. 27(2):145–153.

Sun, B., L. Bi, P. Yang, M. Kahnert & G. Kattawar. 2020. *Invariant Imbedding T-matrix Method for Light Scattering by Nonspherical and Inhomogeneous Particles*, Amsterdam, Netherlands, Elsevier.

Sun, B., P. Yang, G. W. Kattawar & X. Zhang. 2017. Physical-geometric optics method for large size faceted particles. Opt. Express 25:24044-24060.

Tape, W. & J. Moilanen. 2006. *Atmospheric Halos and the Search for Angle X*, American Geophysical Union.

Tsang, L., J. A. Kong, K.-H. Ding & C. O. Ao. 2000. *Scattering of Electromagnetic Waves: Theories and Applications*. New York, Wiley.

van de Hulst, H. C. 1957. *Light Scattering by Small Particles*. New York: John Wiley & Sons.

Waterman, P. C. 1971. Symmetry, unitarity, and geometry in electromagnetic scattering, *Phys.. Rev. D* 3(4):825–839.

Wei, J., T. Ren, T., P. Yang, S. F. DiMarco & E. Mlawer. 2021. An improved ocean surface albedo computational scheme: Structure and performance. J. Geophys. Res.: Oceans. 126, e2020JC016958. https://doi.org/10.1029/2020JC016958.

Wendling, P., R. Wendling & H. K. Weickmann. 1979. Scattering of solar radiation by hexagonal ice crystals. Appl. Opt. 18:2663–2671.

Winker, D. M. & C. R. Trepte. 1998. Laminar cirrus observed near the tropical tropopause by LITE. Geophys. Res. Lett. 35:3351-3354.

Yang, P. & K. N. Liou. 1996: Geometric-optics-integral-equation method for light scattering by nonspherical ice crystals. Appl. Opt. 35:6568-6584.

Yang, P. & K. N. Liou. 1997. Light scattering by hexagonal ice crystals: Solution by a ray-by-ray integration algorithm, J. Opt. Soc. Amer. A. 14:2278-2289.

Yang, P., G. Hong, G. W. Kattawar, P. Minnis & Y. Hu. 2008. Uncertainties associated with the surface texture of ice particles in satellite-based retrieval of cirrus clouds: Part II. Effect of particle surface roughness on retrieved cloud optical thickness and effective particle size. IEEE Trans. Geosci. Remote Sens. 46:1948-1957.

Yang, P., G. Hong, A. E. Dessler, S. C. Ou, K. N. Liou, P. Minnis & Hashvardhan. 2010. Contrails and Induced Cirrus: Optics and Radiation. Bull. Am. Meteorol. Soc. 91:473-478.

Yang, P., S. Hioki, M. Saito, C.-P. Kuo, B. A. Baum &K.-N. Liou. 2018. A review of ice cloud optical property models for satellite remote sensing. Atmosphere 9:499. DOI 10.3390/atmos9120499

Yang, P., J. Ding, R. L. Panetta, K.-N. Liou, G. W. Kattawar, & M. I. Mishchenko. 2019. On the convergence of numerical computations for both exact and approximate solutions for electromagnetic scattering by nonspherical dielectric particles. Prog. Electromagn. Res. 164:27-61.

Yi, B., P. Yang, B. A. Baum, T. L'Ecuyer, L. Oreopoulos, E. J. Mlawer, A. J. Heymsfield & K.-N. Liou. 2013. Influence of ice particle surface roughening on the global cloud radiative effect. J. Atmos. Sci. 70:2794-2807.